

Global gyrokinetic particle simulations of microturbulence in W7-X and LHD stellarators

Cite as: Phys. Plasmas **27**, 082305 (2020); doi: 10.1063/5.0014198

Submitted: 19 May 2020 · Accepted: 22 July 2020 ·

Published Online: 13 August 2020



View Online



Export Citation



CrossMark

H. Y. Wang,^{1,2} I. Holod,^{2,3} Z. Lin,^{2,a)}  J. Bao,^{2,4} J. Y. Fu,¹ P. F. Liu,² J. H. Nicolau,²  D. Spong,⁵  and Y. Xiao⁶ 

AFFILIATIONS

¹Fusion Simulation Center, Peking University, Beijing 100871, China

²Department of Physics and Astronomy, University of California, Irvine, California 92697, USA

³Max Planck Computing and Data Facility, Giessenbachstrasse 2, 85748 Garching, Germany

⁴Institute of Physics, Chinese Academy of Science, Beijing 100190, China

⁵Oak Ridge National Laboratory, Oak Ridge, Tennessee 37831, USA

⁶Institute for Fusion Theory and Simulation, Department of Physics, Zhejiang University, Hangzhou 310027, China

^{a)}Author to whom correspondence should be addressed: zhihongl@uci.edu

ABSTRACT

Global gyrokinetic particle simulations of electrostatic ion temperature gradient (ITG) instability show that the most unstable eigenmode is localized to some magnetic fieldlines or discrete locations on the poloidal plane in the Wendelstein 7-X (W7-X) stellarator due to its mirror-like magnetic fields, which vary strongly in the toroidal direction and induce coupling of more toroidal harmonics (n) to form the linear eigenmode than in the Large Helical Device (LHD) stellarator. Nonlinear electrostatic simulation results show that self-generated zonal flows are the dominant saturation mechanism for the ITG instabilities in both the LHD and W7-X. Furthermore, radial widths of the fluctuation intensity in both the LHD and W7-X are significantly broadened from the linear phase to the nonlinear phase due to turbulence spreading. Finally, nonlinear spectra in the W7-X are dominated by low- n harmonics, which can be generated both by nonlinear toroidal coupling of high- n harmonics and by linear toroidal coupling with large amplitude zonal flows due to the 3D equilibrium magnetic fields.

Published under license by AIP Publishing. <https://doi.org/10.1063/5.0014198>

I. INTRODUCTION

The stellarator^{1–3} is an attractive fusion reactor concept with steady state operation and reduced risk of disruptions since no plasma current drive is needed. However, the intrinsically 3D magnetic equilibrium could destroy the conservation of canonical angular momentum, allowing particle orbits to drift far away from magnetic flux surfaces. The breaking of the toroidal symmetry could enhance collisional (neoclassical) transport, increase plasma flow damping, and modify the structure and coupling of both macro- and micro-instabilities. Recently, design and optimization of stellarators with quasi-symmetry have greatly improved the plasma confinement. In particular, the drift-optimized quasi-isodynamic Wendelstein 7-X (W7-X)⁴ has achieved plasma confinement approaching the performance of axisymmetric tokamaks. Originally designed for magnetohydrodynamic (MHD) stability, the Large Helical Device (LHD)⁵ has also found an optimized operation regime, where a strong inward shift of magnetic axis reduces the neoclassical transport to the level of an advanced stellarator⁶ or an approximately quasi-omnigenous stellarator.^{7,8}

With reduced neoclassical transport, turbulent transport becomes a critical issue for the plasma confinement in stellarators. For example, turbulent transport has been conjectured to account for a significant fraction of core transport and for the majority of edge transport in W7-X experiments.⁹ In fact, transport coefficients measured from experiments are much larger than those predicted by the neoclassical theory, which indicates that turbulent transport plays a dominant role.¹⁰ Core plasma fluctuations measured by phase contrast imaging (PCI)¹¹ show characteristics of ion temperature gradient (ITG) and trapped electron mode (TEM) turbulence. Therefore, it is important to understand the properties of microturbulence in the stellarators, which are complicated by the 3D equilibrium. Furthermore, the interactions between neoclassical and turbulent transport in stellarators and the extrapolation to the reactor regime have not been widely studied by theory or simulations.

Some progress has been made for gyrokinetic simulations of the microturbulence in stellarators. The gyrokinetic continuum flux-tube code GKV has been used to carry out extensive simulations of

stellarators, e.g., finding isotope and collisional effects on the turbulent transport and zonal-flow generation by the TEM turbulence in the LHD.¹² Another gyrokinetic continuum code GENE has been used to carry out radially local simulations of the microturbulence in stellarators, finding a broadband turbulence due to the co-existence of multiple ITG modes.¹³ Effects of 3D geometry on zonal flows dynamics¹⁴ and turbulent transport¹⁵ have been studied. Effects of radial electric fields on the linear ITG instabilities in the W7-X and LHD have also been studied using the global gyrokinetic particle-in-cell code EUTERPE.¹⁶ A full-f gyrokinetic code, GT5D, has been used to study the collisionless damping of zonal flows in the LHD.¹⁷

Previous nonlinear gyrokinetic simulations of the microturbulence in stellarators have been performed in a flux-tube or radially local geometry. However, flux-tube simulations do not properly treat the coupling of multiple toroidal harmonics induced by the 3D magnetic fields in the stellarators, which require full flux-surface simulations. The helically trapped particles can drift far across flux-surfaces and thus require radially nonlocal simulations. In this work, global gyrokinetic particle simulations of the microturbulence are carried out in the LHD and W7-X stellarators by using the gyrokinetic toroidal code (GTC).¹⁸ The capability of simulating 3D equilibrium has been developed in the GTC, which has been applied to simulate toroidal Alfvén eigenmodes in the LHD,¹⁹ ITG/TEM turbulence and kinetic ballooning mode (KBM) turbulence in the DIII-D tokamak with 3D resonant magnetic perturbations (RMPs),²⁰ and effects of magnetic islands on bootstrap current²¹ and on microturbulence.^{22,23} An early GTC version has been used in the simulations of neoclassical transport and ambipolar electric fields for the design of a compact stellarator.^{24–27}

A feature in the GTC is the global field-aligned mesh,²⁸ which provides the maximal computational efficiency without making any geometry approximation.²⁹ In particular, the computational cost of GTC simulations using the field-aligned mesh is proportional to n^2 , where n is the most unstable toroidal mode number. For comparison, other global simulation codes using toroidal mode decomposition or ballooning mode representation have a computational cost proportional to n^3 when interactions between all unstable toroidal harmonics in stellarators must be treated. Therefore, using the global field-aligned mesh can reduce computational requirements by two orders of magnitude since the most unstable ITG mode in the W7-X is $n \approx 200$ (see Sec. III).

This paper reports the development and verification for the first nonlinear global gyrokinetic simulations of the microturbulence in the LHD and W7-X stellarators. Linear GTC simulations show that the electrostatic ITG eigenmode structure is extended in the magnetic field direction but narrow in the perpendicular direction and peaks in bad curvature regions in both LHD and W7-X stellarators. The eigenmode structure is localized at the outer mid-plane in the LHD, similar to that in a tokamak. On the other hand, the eigenmode structure in the W7-X is strongly localized to some magnetic fieldlines or discrete locations on the poloidal plane, which is due to the mirror-like magnetic fields varying strongly in the toroidal direction that induce coupling of more toroidal n -harmonics to form the linear eigenmode. The linear GTC simulation results are in good agreement with the results from EUTERPE simulations of the same ITG eigenmode in the W7-X using identical magnetic geometry and plasma profiles.

GTC nonlinear electrostatic simulations show that regulation by self-generated zonal flows is the dominant saturation mechanism for

the ITG instabilities in both LHD and W7-X stellarators. Furthermore, radial widths of the fluctuation intensity in both the LHD and W7-X are significantly broadened from the linear phase to the nonlinear phase due to turbulence spreading. Finally, the nonlinear spectra in the W7-X are dominated by low- n harmonics (e.g., $n = 5, 10,$ and 15), which can be generated both by nonlinear toroidal coupling of high- n harmonics (e.g., $n = 200$ and $n = 205$) and by linear toroidal coupling of these low- n harmonics with large amplitude zonal flows ($n = 0$). Note that the linear toroidal coupling of zonal flows with non-zonal modes is induced by the 3D magnetic fields (e.g., with $n = 5, 10,$ and 15 harmonics) in the stellarators, an interesting new physics that does not exist in the axisymmetric tokamaks.

This paper is organized as follows. The representation of the non-axisymmetric toroidal geometry in the GTC and the electrostatic simulation model are described in Sec. II. The linear simulation results of the ITG in the LHD and W7-X are presented in Sec. III. Nonlinear simulation results of the ITG turbulence in the LHD and W7-X are discussed in Sec. IV. Finally, conclusion and discussions are provided in Sec. V.

II. IMPLEMENTATION OF THE 3D TOROIDAL GEOMETRY AND SIMULATION MODEL IN THE GTC

A. Implementation of 3D toroidal geometry

The GTC uses realistic toroidal equilibrium geometry of fusion experiments^{20,29,30} reconstructed by MHD equilibrium codes including EFIT,³¹ VMEC,³² M3D-C1,³³ and LR_eqML.³⁴ In the current simulations of ITG instabilities in LHD and W7-X stellarators, the GTC uses VMEC equilibria, which assume closed magnetic flux surfaces. The 3D toroidal equilibrium from the VMEC was first implemented in the GTC for simulations of toroidal Alfvén eigenmode instabilities in the LHD,¹⁹ and microturbulence in the DIII-D tokamak with resonant magnetic perturbations (RMPs).²⁰ The VMEC equilibrium data include poloidal current $g(\psi)$, toroidal current $I(\psi)$, and magnetic safety factor $q(\psi)$. The equilibrium geometry and magnetic field data from the VMEC are provided in the form of Fourier series coefficients B_c and B_s in the toroidal direction,

$$B(\psi, \theta, \zeta) = \sum_n [B_c(\psi, \theta, n)\cos(n\zeta) + B_s(\psi, \theta, n)\sin(n\zeta)], \quad (1)$$

where (ψ, θ, ζ) are the poloidal flux, poloidal angle, and toroidal angle, respectively, forming right-handed Boozer coordinates,³⁵ and n is the toroidal harmonic. The Fourier coefficients B_c and B_s are specified on a rectangular equilibrium mesh on the (ψ, θ) poloidal plane. Similarly, the transformations between Boozer coordinates (ψ, θ, ζ) and cylindrical coordinates (R, Φ, Z) are also given by the same form of Eq. (1). Here, R and Z are Cartesian coordinates on the poloidal plane, and Φ is the toroidal angle in cylindrical coordinates. The difference between Φ and ζ is given by the Fourier series with the same form of Eq. (1). The GTC retains rigorously all the ζ -dependence of the magnetic field and the coordinate transformations for simulating 3D toroidal equilibria including stellarators¹⁹ and tokamaks with RMPs.²⁰

Since evaluations of trigonometric functions in Eq. (1) are computationally expensive, the GTC uses quadratic spline interpolation on an equilibrium mesh in the (ψ, θ, ζ) coordinates to efficiently evaluate the 3D equilibrium quantities. The spline coefficients are constructed on the identical mesh in (ψ, θ) as VMEC data, plus a regular toroidal equilibrium mesh along ζ with spline coefficients associated with a particular toroidal grid point being stored by the computing processor

with the corresponding toroidal rank in the toroidal domain decomposition using the Message Passing Interface (MPI). The periodicities of the values and the first derivatives in the θ and ζ directions are enforced by using the periodic boundary condition when constructing the spline functions. An odd number of spline sections in these directions is required due to intrinsic constraints in the periodic quadratic spline algorithm.³⁶

Both the LHD and W7-X have a stellarator symmetry with a number of field periods $N_{fp} = 10$ and 5 , respectively, i.e., all equilibrium quantities have a periodicity of $2\pi/N_{fp}$ in the toroidal direction. Therefore, the equilibrium spline can be constructed on the equilibrium mesh for a field period of $\zeta = [0, 2\pi/N_{fp}]$ with the toroidal periodicity explicitly enforced at $\zeta = 0$ and $2\pi/N_{fp}$. This field period is also used in linear simulations of a single 3D eigenmode using a turbulence mesh as described in Sec. III.

The field-aligned turbulence mesh in the GTC allows a significantly smaller number of parallel grid points to resolve the eigenmode structure along the magnetic field direction, which has been implemented in tokamak simulations.²⁸ However, the breaking of the toroidal symmetry in stellarators requires a much larger number of toroidal grid points in the equilibrium mesh for evaluating 3D equilibrium quantities. If we use the same number of equilibrium toroidal grid points for the turbulence parallel grid points, we would over-resolve the parallel eigenmode structure, which could have numerical issues due to unphysical modes with large parallel wavevectors. Therefore, in the GTC simulations of stellarators, more toroidal grid points in the equilibrium mesh are used than the parallel grid points in the turbulence mesh. We use N_p turbulence mesh in the parallel direction, on which charge density is gathered from particles and Poisson equation is solved.²⁹ We use N_e extra grid points between every two turbulence grid points to construct the equilibrium mesh, on which equilibrium magnetic fields are calculated and used to push particles. Therefore, the total equilibrium grid points in the toroidal direction are $N_p(N_e + 1)$.

B. Electrostatic simulation model

In this work, we assume that the electron response is adiabatic and use electrostatic gyrokinetic equation for ions. The collisionless gyrokinetic equation^{37,38} is

$$\frac{d}{dt}f(\mathbf{X}, \mu, v_{\parallel}, t) = \left[\frac{\partial}{\partial t} + \dot{\mathbf{X}} \cdot \nabla + \dot{v}_{\parallel} \frac{\partial}{\partial v_{\parallel}} \right] f = 0, \quad (2)$$

in which

$$\begin{aligned} \dot{\mathbf{X}} &= v_{\parallel} \mathbf{b} + \mathbf{v}_E + \mathbf{v}_d, \\ \dot{v}_{\parallel} &= -\frac{1}{m} \frac{\mathbf{B}^*}{B} \cdot (\mu \nabla B + Z \nabla \phi). \end{aligned}$$

Here, $f(\mathbf{X}, \mu, v_{\parallel}, t)$ is the distribution function with \mathbf{X} being the gyrocenter position, μ the magnetic moment, and v_{\parallel} the parallel velocity, Z is the ion charge, and m is the ion mass. \mathbf{B} is the equilibrium magnetic field, $\mathbf{B}^* = \mathbf{B} + \frac{Bv_{\parallel}}{\Omega} \nabla \times \mathbf{b}$, and $\mathbf{b} = \frac{\mathbf{B}}{B} \mathbf{v}_E$ and \mathbf{v}_d are the $\mathbf{E} \times \mathbf{B}$ drift velocity and magnetic drift velocity, respectively. In this work, we keep the zonal flows generated by the ITG turbulence but neglect the equilibrium radial electric fields associated with the neoclassical ambipolarity in the non-axisymmetric systems. The ITG turbulent transport is automatically ambipolar because of quasi-neutrality.

In order to reduce the particle noise in simulations, the δf method³⁹ is used in this work. The ion gyrocenter distribution function $f = f_0 + \delta f$ is decomposed into equilibrium part f_0 and perturbed part δf . The propagator in Eq. (2) is separated into an equilibrium part L_0 and a perturbed part δL . So Eq. (2) can be expressed as $(L_0 + \delta L)(f_0 + \delta f) = 0$, in which

$$\begin{aligned} L_0 &= \frac{\partial}{\partial t} + (v_{\parallel} \mathbf{b} + \mathbf{v}_d) \cdot \nabla - \frac{1}{m} \frac{\mathbf{B}^*}{B} \cdot (\mu \nabla B) \frac{\partial}{\partial v_{\parallel}}, \\ \delta L &= \mathbf{v}_E \cdot \nabla - \frac{1}{m} \frac{\mathbf{B}^*}{B} \cdot Z \nabla \phi \frac{\partial}{\partial v_{\parallel}}. \end{aligned}$$

The equilibrium distribution function f_0 is determined by $L_0 f_0 = 0$, which yields the neoclassical solution f_0 . The perturbed distribution function is determined by $(L_0 + \delta L)\delta f = -\delta L f_0$. We define the particle weight as $w = \delta f/f$, which is governed by

$$\frac{d}{dt}w = (1-w) \left[-\mathbf{v}_E \cdot \frac{\nabla f_0}{f_0} + \frac{Z}{mf_0} \frac{\mathbf{B}^*}{B} \cdot \nabla \phi \frac{\partial f_0}{\partial v_{\parallel}} \right]. \quad (3)$$

To solve Eq. (3), an analytical form of f_0 is needed. Since the neoclassical solution f_0 is not generally available and needs to be solved numerically,⁴⁰ we approximate f_0 as a local Maxwellian in Eq. (3). Therefore, neoclassical effects are not taken into account in this work since the neoclassical term of $\mathbf{v}_d \cdot \nabla f_0$ does not appear in Eq. (3).

In magnetic coordinates, guiding center equations of motion in electrostatic simulations are as follows:^{41,42}

$$\begin{aligned} \dot{\psi} &= \frac{c}{Z} \frac{\partial \epsilon}{\partial B} \left(\frac{I}{D} \frac{\partial B}{\partial \zeta} - \frac{g}{D} \frac{\partial B}{\partial \theta} \right) + \frac{cI}{D} \frac{\partial \phi}{\partial \zeta} - \frac{cg}{D} \frac{\partial \phi}{\partial \theta}, \\ \dot{\theta} &= \frac{v_{\parallel} B (1 - \rho_c g')}{D} + c \frac{g}{D} \left[\frac{1}{Z} \frac{\partial \epsilon}{\partial B} \frac{\partial B}{\partial \psi} + \frac{\partial \phi}{\partial \psi} \right], \\ \dot{\zeta} &= \frac{v_{\parallel} B (q + \rho_c I')}{D} - c \frac{I}{D} \left[\frac{1}{Z} \frac{\partial \epsilon}{\partial B} \frac{\partial B}{\partial \psi} + \frac{\partial \phi}{\partial \psi} \right], \\ \dot{\rho}_{\parallel} &= -\frac{(1 - \rho_c g')}{D} \left[\frac{1}{Z} \frac{\partial \epsilon}{\partial B} \frac{\partial B}{\partial \theta} + \frac{\partial \phi}{\partial \theta} \right] - \frac{(q + \rho_c I')}{D} \left[\frac{1}{Z} \frac{\partial \epsilon}{\partial B} \frac{\partial B}{\partial \zeta} + \frac{\partial \phi}{\partial \zeta} \right], \end{aligned}$$

where

$$D = gq + I + \rho_c (gI' - Ig').$$

Here, $I' \equiv \frac{dI}{d\psi}$ and $g' \equiv \frac{dg}{d\psi}$ are radial derivatives of poloidal and toroidal currents. The modified parallel canonical momentum is $\rho_c \approx \rho_{\parallel}$, with $\rho_{\parallel} = \frac{v_{\parallel}}{\Omega} = \frac{m\epsilon}{ZB} v_{\parallel}$, and $\frac{\partial \epsilon}{\partial B} = \mu + \frac{Z^2}{mc^2} \rho_{\parallel}^2 B$ is used for short. Those terms associated with ϕ are nonlinear terms used only in nonlinear simulations. The perturbed electrostatic potentials are gyro-averaged for ions.

III. LINEAR SIMULATION OF ITG INSTABILITY IN STELLARATORS

A. ITG instability in the LHD

The equilibrium magnetic geometry and plasma profiles of the LHD stellarator used in this work are adapted from Ref. 16. The LHD stellarator has a number of field periods $N_{fp} = 10$, i.e., all equilibrium quantities including magnetic fields and metric tensors are symmetric under the rotation of 0.2π in the toroidal direction. The 3D magnetic field plotted on the last closed flux surface (with a poloidal flux ψ_X) is

shown in Fig. 1(a), which shows a helical pole number of $l=2$ and a strong variation of magnetic fields and flux surface shapes in the toroidal direction. The 2D contours of the flux surface with a poloidal flux $\psi_d = 0.18$, which is normalized by ψ_X , are plotted in Fig. 1(b) for $\zeta/\pi = 0, 0.05, 0.1, \text{ and } 0.15$. It shows that the magnetic axis has a nearly fixed position on the poloidal planes (e.g., almost circular from the top view), which is a main character of one kind of stellarator called heliotron.^{43,44} Because of the field period symmetry, the equilibrium magnetic fields contain only toroidal harmonics of $n = kN_{fp}$, where k is a non-negative integer. The amplitudes of the magnetic field harmonics

B_c for $n = 0, 10, 20, \text{ and } 30$ at the poloidal angle $\theta = 0$ are plotted in Fig. 1(e) as a function of the normalized poloidal flux ψ , which shows that the dominant non-axisymmetric part of the magnetic field is the $n = 10$ harmonic. In Figs. 1(c) and 1(d), the cosines and sines Fourier series coefficients of the $n = 10$ harmonic are also plotted on the (ψ, θ) surface, which show a strong poloidal harmonic of $m = 2$.

The magnetic field pitch in the stellarator is often characterized by a rotational transform ι , where $\iota = 1/q$ and q is the safety factor representing the number of toroidal turns per poloidal turn of the magnetic field line on a flux surface. The radial profile of ι is plotted in

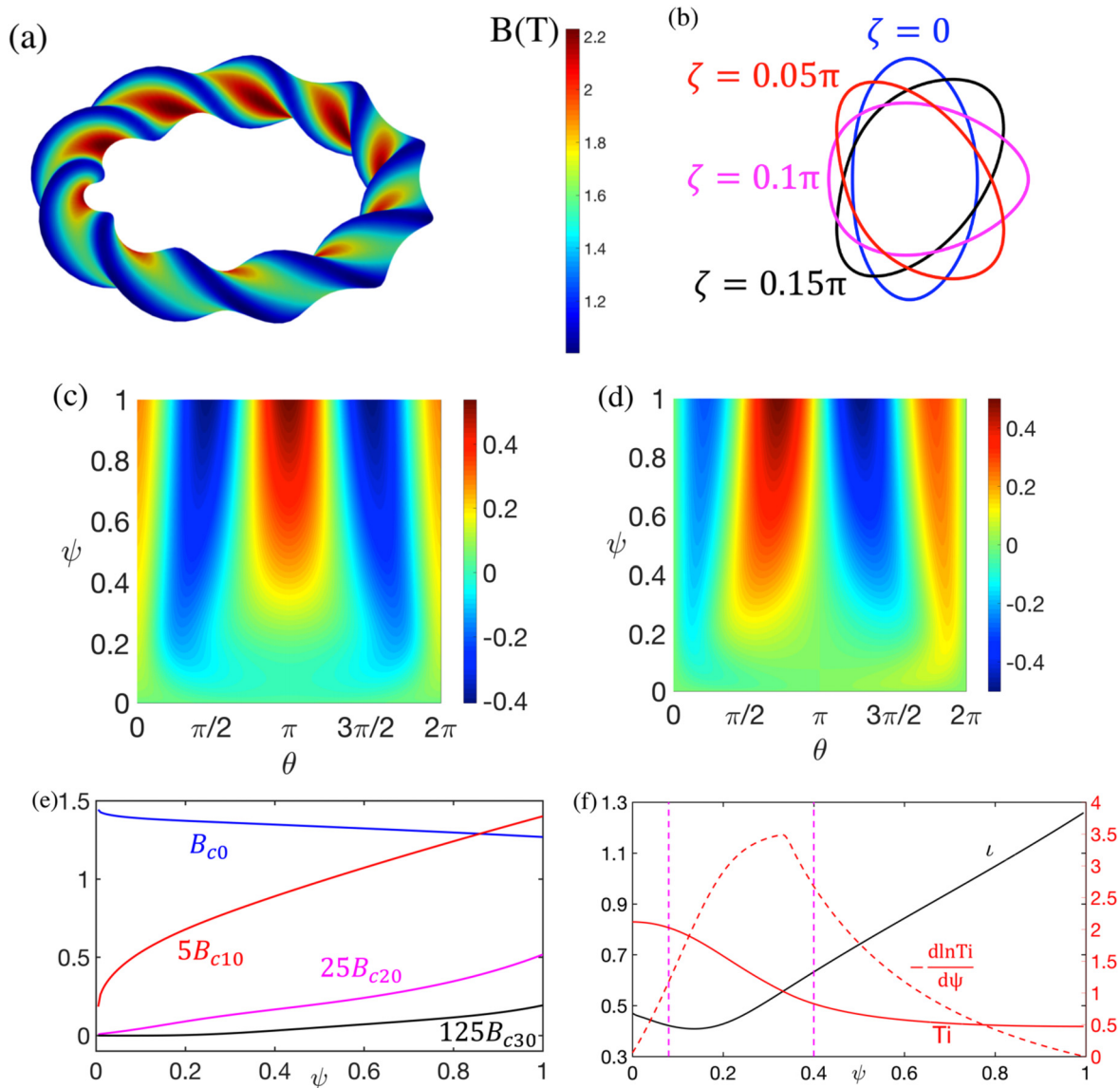


FIG. 1. (a) Real space 3D plot of magnetic field B on the last closed flux surface of the LHD. (b) Real space 2D poloidal contours of flux surface $\psi = 0.18\psi_X$ at $\zeta = 0$ (blue), $\zeta = 0.05\pi$ (red), $\zeta = 0.1\pi$ (magenta), and $\zeta = 0.15\pi$ (black). (c) 2D plot of $n = 10$ cosines Fourier series coefficients $B_{c10}(\psi, \theta)$. (d) 2D plot of $n = 10$ sines Fourier series coefficients $B_{s10}(\psi, \theta)$. (e) Radial profiles for Fourier cosines series coefficients of the magnetic field at $\theta = 0$. Amplitudes of B_{c0} , B_{c20} , and B_{c30} are amplified. (f) Radial profiles for equilibrium ion temperature T_i (red solid line), ion temperature gradient $-\frac{d \ln T_i}{d\psi}$ (red dashed line), and rotational transform ι (black). The simulation range is marked by vertical dashed magenta lines: $\psi_{inner} = 0.08\psi_X$ and $\psi_{outer} = 0.40\psi_X$.

Fig. 1(f), which indicates that the magnetic shear is strong (except for the radial location with the minimal ι). The boundaries of the simulation domain are $\psi_{\text{inner}} = 0.08 \psi_X$ and $\psi_{\text{outer}} = 0.40 \psi_X$, which are marked by two dashed lines in Fig. 1(f), where the ion temperature profile T_i and its gradient are also plotted. We assume uniform electron temperature T_e , electron density n_e , and ion density n_i . The electron response is adiabatic in the current electrostatic simulation of the ITG. The ion species is proton and the ion dynamic is described by the gyrokinetic equation. When a particle goes outside the radial boundaries in the simulation, it is put back to the simulation domain and its weight is set to zero, which could result in a small net charge. The volume-averaged net charge is subtracted from the charge density used for solving the Poisson equation. So the particles that go outside the radial simulation domain will not affect the self-consistent electrostatic potential, but the total marker number is kept constant. There are non-vanishing temperature gradients at the radial boundaries.

However, there are buffer zones near both boundaries, where fluctuating potential is smoothly suppressed to be zero at the boundaries. All mode diagnostics are done on the $\psi_d = 0.18$ flux surface, where $\iota = 0.42$. Other parameters used in the simulations are as follows: magnetic field on axis $B_0 = 1.45$ T, electron temperature $T_e = 1$ keV, and major radius $R_0 = 3.96$ m, which corresponds to the outward-shifted magnetic configuration of the LHD stellarator.^{45,46} The simulation time step size is $\Delta t = 0.01 R_0 / C_s$, and $C_s = \sqrt{T_e / m_i}$. Growth rates and real frequencies of the simulations in this section are normalized by $C_s / R_0 = 8.37 \times 10^4 \text{ s}^{-1}$.

Since the LHD stellarator has a number of field periods $N_{fp} = 10$, there exists ten linear eigenmode families. Each of the i th eigenmode family has multiple frequencies (eigenstates) and consists of coupled toroidal harmonics $n = i + 10k$, where k is a positive integer and $i = 0, 1, 2, \dots, 9$. The first eigenmode family ($i = 0$) can be simulated using a partial torus geometry⁴⁷ with one field period of the toroidal domain,

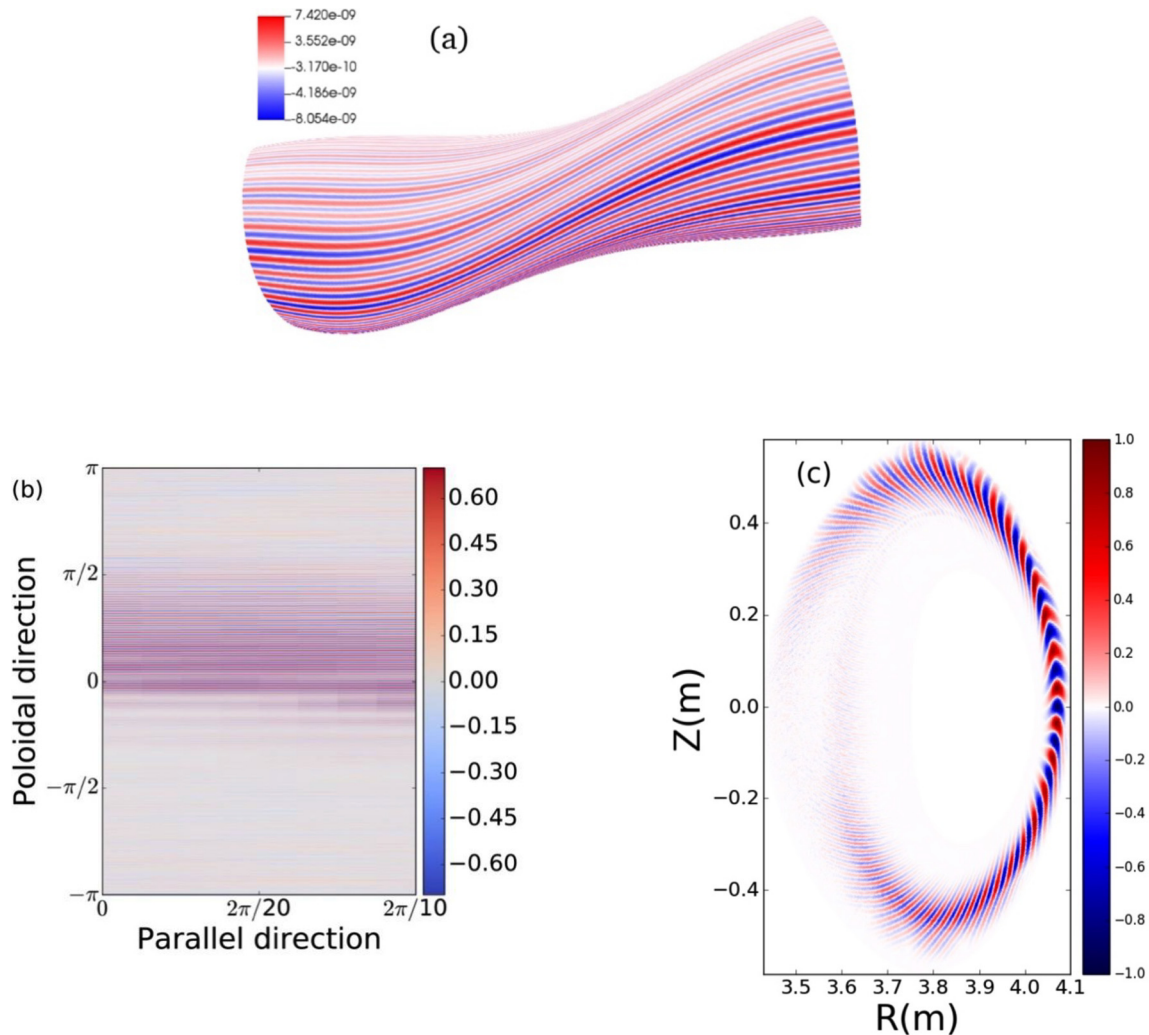


FIG. 2. Contour plots of electrostatic potential $\delta\phi$ (arbitrary unit) on a flux surface plotted in the 3D real space (panel a), on the flux surface (panel b), and on the $\zeta = 0$ poloidal plane (panel c) from GTC linear simulations of a single ITG eigenmode in the LHD.

$\zeta = [0, 2\pi/10]$. Other eigenmodes have also been simulated and exhibit similar frequencies, growth rates, and mode structures as the $i=0$ eigenmode family described on this subsection.

We first carry out studies of numerical convergence for the parallel grid number of the turbulence mesh and the toroidal grid number of the equilibrium mesh. To get these two kinds of grid numbers converged, we first keep the turbulence grid number $N_p = 9$ but vary N_e to increase the equilibrium grid number. The growth rates and frequencies from simulations using $N_e = 0, 2, 6,$ and 10 indicate that $N_e = 2$ is enough for convergence when $N_p = 9$. Then, we vary the parallel grid number of the turbulence mesh N_p by fixing the toroidal grid number of the equilibrium mesh $N_p(N_e + 1) = 25$ or 27 , and simulation results show that $N_p = 9$ and $N_e = 2$ are sufficient for convergence in the LHD simulations using one field period. For linear simulations, we use 110 radial grid points, 2700 poloidal grid points, and 10 ions per cell. The numbers of perpendicular grid points are chosen to resolve sufficiently the most unstable eigenmode after rigorous convergence studies. The same numbers of grid points are then used in both linear and

nonlinear simulations although nonlinear simulations typically require smaller numbers of grid points due to the inverse cascade of fluctuation intensity.

The eigenmode structure in the 3D real space is shown in panel (a) of Fig. 2, on the (α, ζ) plane in panel (b), where $\alpha = \theta - \zeta/q$ represents the direction perpendicular to the field lines and ζ parallel to the field lines, and on poloidal plane at $\zeta = 0$ in panel (c), where the color represents the amplitude of electrostatic potential ϕ . The eigenmode structure is narrow in the perpendicular direction but extended in the magnetic field direction. The mode amplitude peaks at the outer mid-plane, i.e., the bad curvature region. Figure 2 shows that the ITG mode structure in the LHD is similar to that in a tokamak, except that a single eigenmode in the stellarator is a linear superposition of many toroidal n harmonics.

The 2D spectrum of the eigenmode on the diagnosed flux surface is shown in Fig. 3(a), which is calculated by decomposing the electrostatic potential into toroidal and poloidal harmonics in the magnetic coordinates,

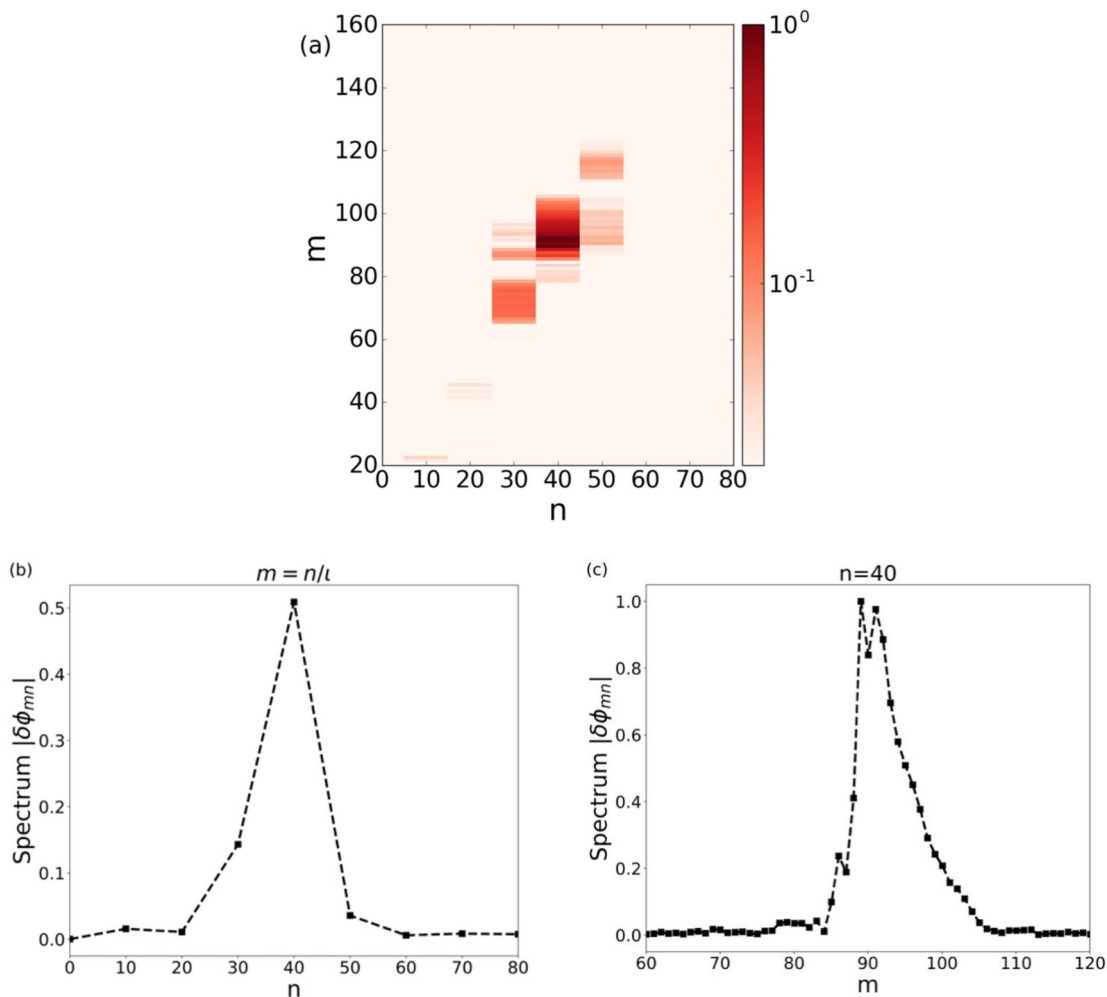


FIG. 3. (a) 2D spectrum $|\delta\phi_{mn}|$ on the diagnosed flux surface in GTC linear simulation of a single ITG eigenmode in the LHD. (b) Toroidal spectrum $|\delta\phi_n|$ with $m = n/l$ on the diagnosed flux surface. (c) Poloidal spectrum $|\delta\phi_m|$ with $n = 40$ on the diagnosed flux surface.

$$\phi(\psi_d, \theta, \zeta) = \sum_{n,m} \phi_{mn}(\psi_d) e^{i(m\theta - n\zeta)}. \quad (4)$$

Figure 3(a) shows that $n=40$ is the dominant toroidal harmonic, which couples with $n=30$ and 50 harmonics. The toroidal spectrum, which is a cut along the $m = n/l$ line of the 2D spectrum, is given in Fig. 3(b). The poloidal spectrum for the dominant $n = 40$ harmonic in Fig. 3(c) is a cut along the $n=40$ line of the 2D spectrum. Figure 3 shows that $n = 30, 40,$ and 50 are the unstable n harmonics and that for the most unstable $n = 40$ harmonic, the dominant m harmonics range is $m = [85, 100]$. On the diagnosed flux surface, the range of each unstable harmonics $[n, m]$ is $[n \pm \Delta n, m \pm \Delta m]$, which results in the three discrete structures in the 2D spectrum. For the dominant

toroidal harmonic $n=40$, the growth rate is $\gamma = 2.84 \times 10^4 \text{ s}^{-1} = 0.345 C_s/R_0$ and the real frequency is $\omega = 2.37 \times 10^5 \text{ s}^{-1} = 2.84 C_s/R_0$. We note that the measured real frequency and growth rate are only for the most unstable eigenmode. There could be subdominant modes in the initial value simulations.

B. ITG instability in the W7-X

The equilibrium magnetic geometry and plasma profiles of the W7-X stellarator used in this work are adapted from Ref. 16. The W7-X stellarator has a number of field periods $N_{fp} = 5$, which means that all equilibrium quantities are symmetric under the rotation of 0.4π in the toroidal direction. The 3D magnetic field on the last closed

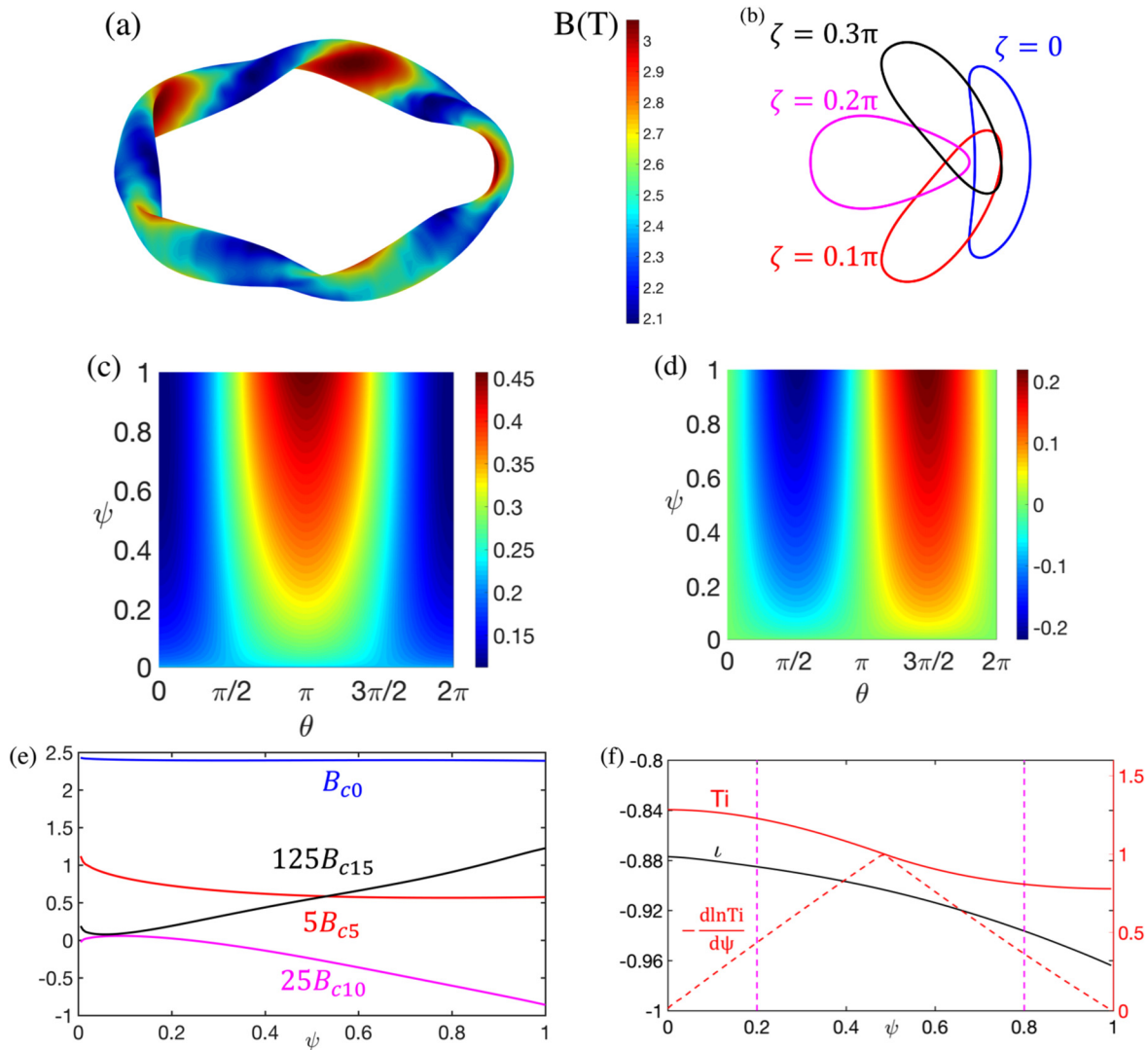


FIG. 4. (a) Real space 3D plot of magnetic field B on the last closed flux surface of W7-X. (b) Real space 2D poloidal contours of flux surface $\psi = 0.49\psi_X$ at $\zeta = 0$ (blue), $\zeta = 0.1\pi$ (red), $\zeta = 0.2\pi$ (magenta), and $\zeta = 0.3\pi$ (black). (c) 2D plot of $n = 5$ cosines Fourier series coefficients $B_{c5}(\psi, \theta)$. (d) 2D plot of $n = 5$ sines Fourier series coefficients $B_{s5}(\psi, \theta)$. (e) Radial profiles for Fourier series cosines coefficients of magnetic field at $\theta = 0$. Amplitudes of B_{c5} , B_{c10} , and B_{c15} are amplified. (f) Radial profiles for ion temperature T_i (red solid line), ion temperature gradient $-\frac{d \ln T_i}{d\psi}$ (red dashed line), and rotational transform ι (black). The simulation range is marked out by magenta lines: $\psi_{inner} = 0.2\psi_X$ and $\psi_{outer} = 0.8\psi_X$.

flux surface is plotted in Fig. 4(a), which shows a helical pole number of $l=2$ and a mirror-like magnetic field in the toroidal direction. The 2D shapes of the flux surface at the poloidal flux $\psi_a=0.49$, which is normalized by ψ_x of the last closed flux surface, are plotted in Fig. 4(b) for $\zeta/\pi = 0, 0.1, 0.2,$ and 0.3 . The magnetic axis does not have a fixed position on the poloidal planes; rather, it rotates in the toroidal direction.

Due to the $N_{fp}=5$ in the W7-X, the equilibrium magnetic fields contain only toroidal harmonics of $n=kN_{fp}$, where k is a non-negative

integer. The amplitudes of the magnetic field harmonics B_c for $n=0, 5, 10,$ and 15 at the poloidal angle $\theta=0$ are plotted in Fig. 4(e) as a function of the poloidal flux ψ , which shows that the dominant non-axisymmetric part of the magnetic field is the $n=5$ harmonic. The cosines and sines Fourier series coefficients of the $n=5$ harmonic on the (ψ, θ) surface are given in Figs. 4(c) and 4(d), respectively, which show the dominant poloidal harmonic of $m=1$.

The radial profile of the rotational transform, ι , is plotted in Fig. 4(f), which indicates that the magnetic shear in the W7-X is very

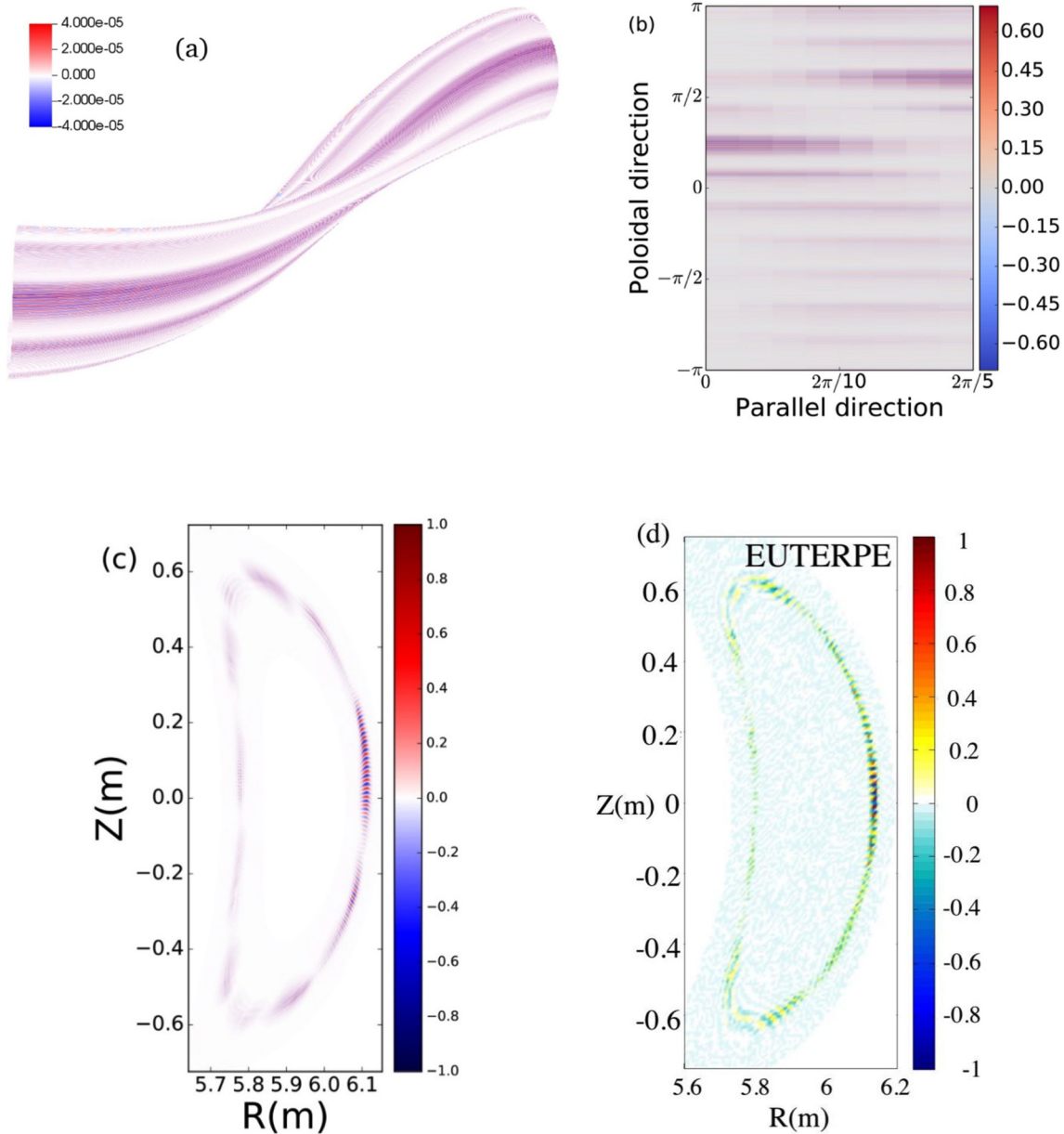


FIG. 5. Contour plots of electrostatic potential $\delta\phi$ (arbitrary unit) on a flux surface in the 3D real space (panel a), on the flux surface (panel b), and on a Boozer toroidal angle $\zeta = 0$ poloidal plane (panel c) from GTC linear simulation of a single ITG eigenmode in the W7-X, and on a cylindrical angle $\Phi = 0$ poloidal plane (panel d) from EUTERPE linear simulation of the same mode in the same equilibrium.

weak. The boundaries of the simulation domain are $\psi_{\text{inner}} = 0.2\psi_X$ and $\psi_{\text{outer}} = 0.8\psi_X$, as marked by two dashed lines in Fig. 4(f), where the ion temperature profile T_i and its gradient are also plotted. We assume uniform electron temperature T_e , electron density n_e , and ion density n_i . The ion species, electron response, and boundary conditions of particles and fluctuating potential are the same as in the LHD simulations. Other parameters used in the simulations are as follows: magnetic field on axis $B_0 = 2.4$ T, major radius $R_0 = 5.62$ m, and $T_e = 1$ keV. The simulation time step size is $\Delta t = 0.01R_0/C_s$. Growth rates and real frequencies of the simulations in this section are normalized by $C_s/R_0 = 5.51 \times 10^4 \text{ s}^{-1}$.

In the W7-X, there are five linear ITG eigenmode families. One field period, i.e., one-fifth torus in the toroidal direction $\zeta = [0, 2\pi/5]$, is used in the following GTC simulations of the first eigenmode family ($i = 0$) with coupled toroidal harmonics of $n = [0, 5, 10, \dots]$. Other eigenmodes have also been simulated and exhibit similar frequencies, growth rates, and mode structures as the $i = 0$ eigenmode family

described in this subsection. First, we study the convergence in the parallel grid number of the turbulence mesh and the toroidal grid number of the equilibrium mesh. The growth rates and frequencies from simulations using $N_e = 0, 2, 6,$ and 10 show that $N_e = 2$ is enough for the convergence when $N_p = 9$. Then, the parallel grid number of the turbulence mesh is varied, but the total toroidal grid number of the equilibrium mesh is kept at 25 or 27, which indicates that $N_p = 9$ and $N_e = 2$ are sufficient for the convergence. For linear simulations, we use 121 radial grid points, 4400 poloidal grid points, and 10 ions per cell.

The eigenmode structure in the 3D real space is shown in panel (a) of Fig. 5, on the flux surface $\psi_d = 0.49$ in panel (b), and on the poloidal plane at $\zeta = 0$ in panel (c). The eigenmode amplitude peaks at the ψ_d flux surface, where the dominant toroidal harmonic is $n = 200$. The mode structure is localized in the bad curvature region of the W7-X and extended in the magnetic field direction. Compared with that in the LHD, the mode structure in the W7-X has less in-out

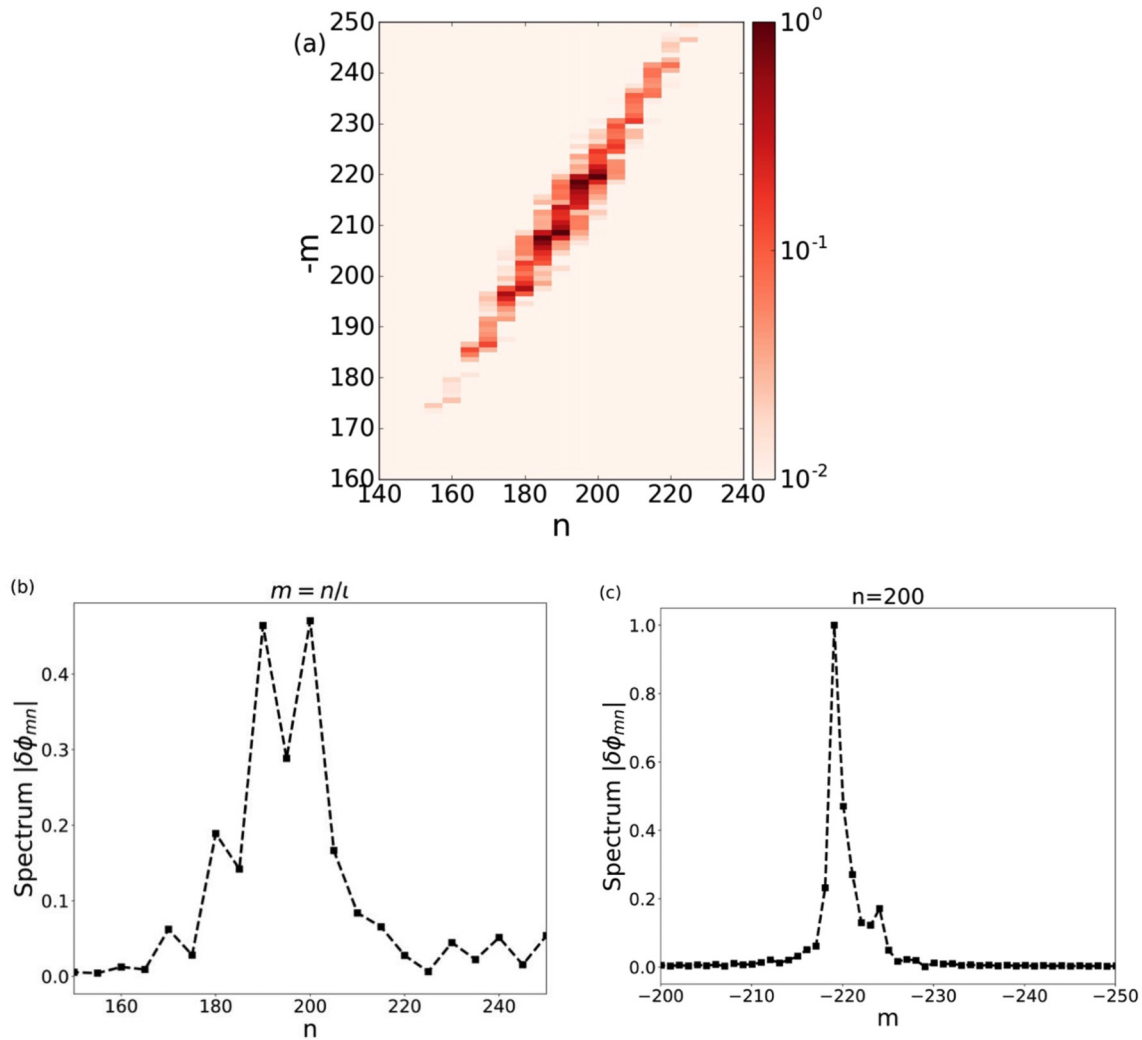


FIG. 6. (a) 2D spectrum $|\delta\phi_{mn}|$ on the diagnosed flux surface in GTC linear simulation of a single ITG eigenmode in the W7-X. (b) Toroidal spectrum $|\delta\phi_n|$ with $m = n/l$ on the diagnosed flux surface. (c) Poloidal spectrum $|\delta\phi_m|$ with $n = 200$ on the diagnosed flux surface.

asymmetry in the poloidal direction, which is due to the weak variations of the magnetic field in the poloidal direction in the W7-X. It is striking that the eigenmode in the W7-X is localized to some magnetic fieldlines, as shown in Fig. 5(a), or within some discrete locations on the poloidal plane, as shown in Fig. 5(c), which is different from that in the LHD [Figs. 2(a) and 2(c)]. The localization of the mode structure is due to the mirror-like magnetic fields varying strongly in the toroidal direction, which induce more toroidal n harmonics to be coupled together to form the linear eigenmode in the W7-X.⁴⁸ This localization of the ITG eigenmode requires a full flux-surface simulation since a flux-tube simulation will give rise to results dependent on the specific magnetic fieldline selected as the simulation domain.

The 2D spectrum of the eigenmode on the ψ_d flux surface is shown in Fig. 6(a). The toroidal spectrum, which is a cut along the $m = n/l$ line of the 2D spectrum, and the poloidal spectrum for the $n = 200$ harmonic are given in Figs. 6(b) and 6(c), respectively. The ratio between dominant toroidal harmonics and poloidal harmonics is close to the rotational transform $l = -0.91$ on the ψ_d flux surface. The dominant toroidal harmonic is around $n = 200$ with the unstable toroidal harmonics range from $n = 180$ to $n = 210$ in the W7-X, which is wider than that in the LHD. Since we only simulate one eigenmode family, harmonic gaps in Fig. 6 are $\Delta n = 5$ and $\Delta m \sim 5$ or 6 for the W7-X with $l \sim -0.91$, compared to that in Fig. 3 with $\Delta n = 10$, $\Delta m \sim 24$ for the LHD with $l \sim 0.42$. So the harmonic gap in the LHD is larger than that in the W7-X.

To verify GTC simulations, we compare GTC linear simulation results to EUTERPE linear simulation results for the same ITG eigenmode family ($i = 0$) using identical W7-X magnetic geometry and plasma profiles in a careful benchmark.⁴⁹ The growth rate measured using the highest amplitude harmonic ($n = 200$ and $m = -219$) from the GTC is $\gamma_{GTC} = 3.43 \times 10^4 \text{ s}^{-1} = 0.623 C_s/R_0$, which agrees very well with $\gamma_{EUTERPE} = 3.38 \times 10^4 \text{ s}^{-1}$ from EUTERPE. The frequency measured using the highest amplitude harmonic ($n = 200$ and $m = -219$) from the GTC is $\omega_{GTC} = 1.57 \times 10^5 \text{ s}^{-1} = 2.85 C_s/R_0$, which agrees reasonably with $\omega_{EUTERPE} = 1.76 \times 10^5 \text{ s}^{-1}$ from EUTERPE. Similar agreement between the GTC and EUTERPE has been obtained when varying η_i (ratio of ion temperature gradient to density gradient) in a careful benchmark.⁴⁹ Similar results have also been obtained later by XGC-S linear electrostatic simulations⁵⁰ of this GTC-EUTERPE benchmark case. The eigenmode structure on the poloidal plane at the Boozer toroidal angle $\zeta = 0$ is shown in Fig. 5(c) from the GTC simulation and in Fig. 5(d) from the EUTERPE simulation on the poloidal plane at the cylindrical angle $\Phi = 0$. The eigenmode structures from both codes exhibit discrete locations of peak mode amplitudes. There are some differences in the details of the mode structures from these two codes. We suspect that these differences are partially due to the different coordinates used in these two codes: the poloidal plane in Fig. 5(d) from the EUTERPE is a flat surface with the cylindrical toroidal angle $\Phi = 0$, but the poloidal plane in Fig. 5(c) from the GTC in a curved surface with the Boozer toroidal angle $\zeta = 0$. Furthermore, the spectra of the perturbed potential $\delta\phi$ are calculated using different coordinates, which may contribute to the small differences of the spectra and real frequencies from the two codes. The GTC decomposes $\delta\phi$ to toroidal and poloidal harmonics using Boozer angles (θ, ζ) in Eq. (4), but EUTERPE decomposes the $\delta\phi$ using real space poloidal and toroidal angles (θ, Φ). Finally, we note that the larger range of the unstable toroidal harmonics in the

W7-X requires more grids in the toroidal and poloidal directions in the EUTERPE simulation to resolve all the unstable toroidal and poloidal harmonics. However, the number of parallel grid points in the GTC is independent of the toroidal harmonics and the number of poloidal grid points is only determined by the maximal poloidal harmonic, thanks to the global field-aligned mesh in the GTC.

IV. NONLINEAR SIMULATIONS OF ITG TURBULENCE IN STELLARATORS

Building on the verifications of linear simulations, GTC nonlinear simulations are carried out in this section to study the ITG saturation mechanism in the LHD and W7-X, using the same geometry and profiles described in Secs. II and III but adding nonlinear terms in the guiding center equation of motion. To study the role of zonal flows as the ITG saturation mechanism in the stellarator,^{51,52} only the first

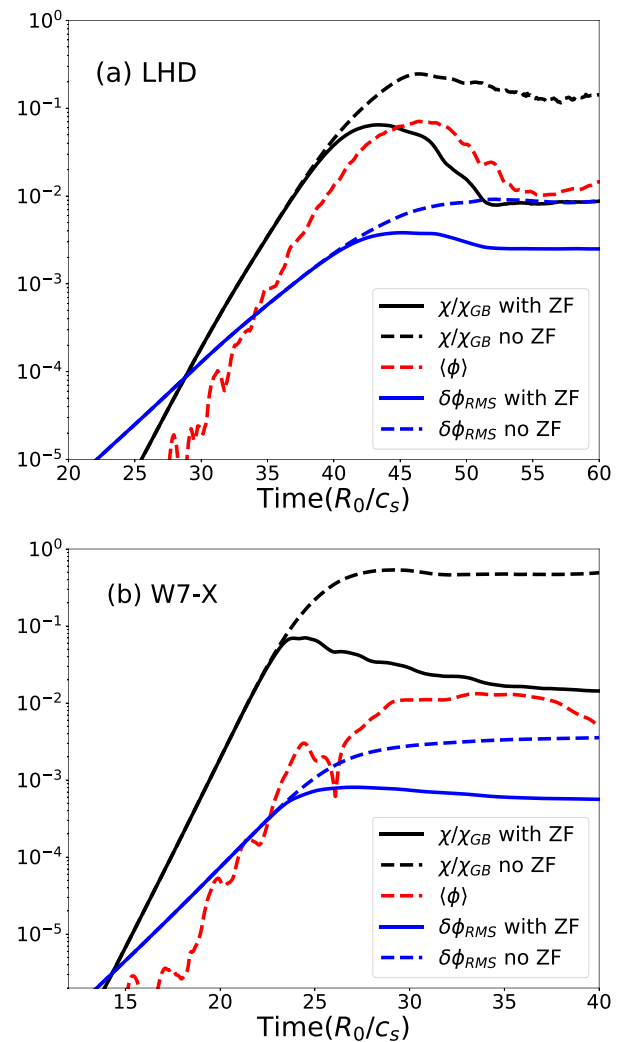


FIG. 7. Time evolution of volume averaged ion heat conductivity (black) and non-zonal electrostatic potential (blue) with (solid) and without (dotted) zonal flows and electrostatic zonal potential (red dotted) in GTC simulations of the ITG in the LHD (upper panel) and the W7-X (lower panel). The electrostatic potential is normalized by Te/e .

eigenmode family ($i = 0$) is kept by using the one field period simulations (i.e., one-tenth of the toroidal domain in the LHD and one-fifth in the W7-X). We have previously found that the saturation of the ITG instabilities in tokamaks is due to the self-generated zonal flows¹⁸ and that nonlinear toroidal coupling⁵³ between unstable eigenmodes is subdominant. We will perform nonlinear simulations including all linear eigenmode families in the future study of turbulent transport in stellarators.

The perturbed electrostatic potential ϕ can be separated into a flux-surface averaged zonal component $\langle\phi\rangle$ with $n = m = 0$ and a

non-zonal component $\delta\phi = \phi - \langle\phi\rangle$. We include self-generated zonal component in the nonlinear simulations but not the equilibrium radial electric field. Collisions are not included in these simulations for simplicity in order to focus on the physics of ITG saturation by zonal flows. For the nonlinear simulations, we use the same grid points and time step size as in the linear simulations but increase particles per cell to 200 to reduce particle noise based on the nonlinear convergence test.

We compare the results from nonlinear simulations with or without the zonal flows in Fig. 7 for both the LHD and W7-X, where the

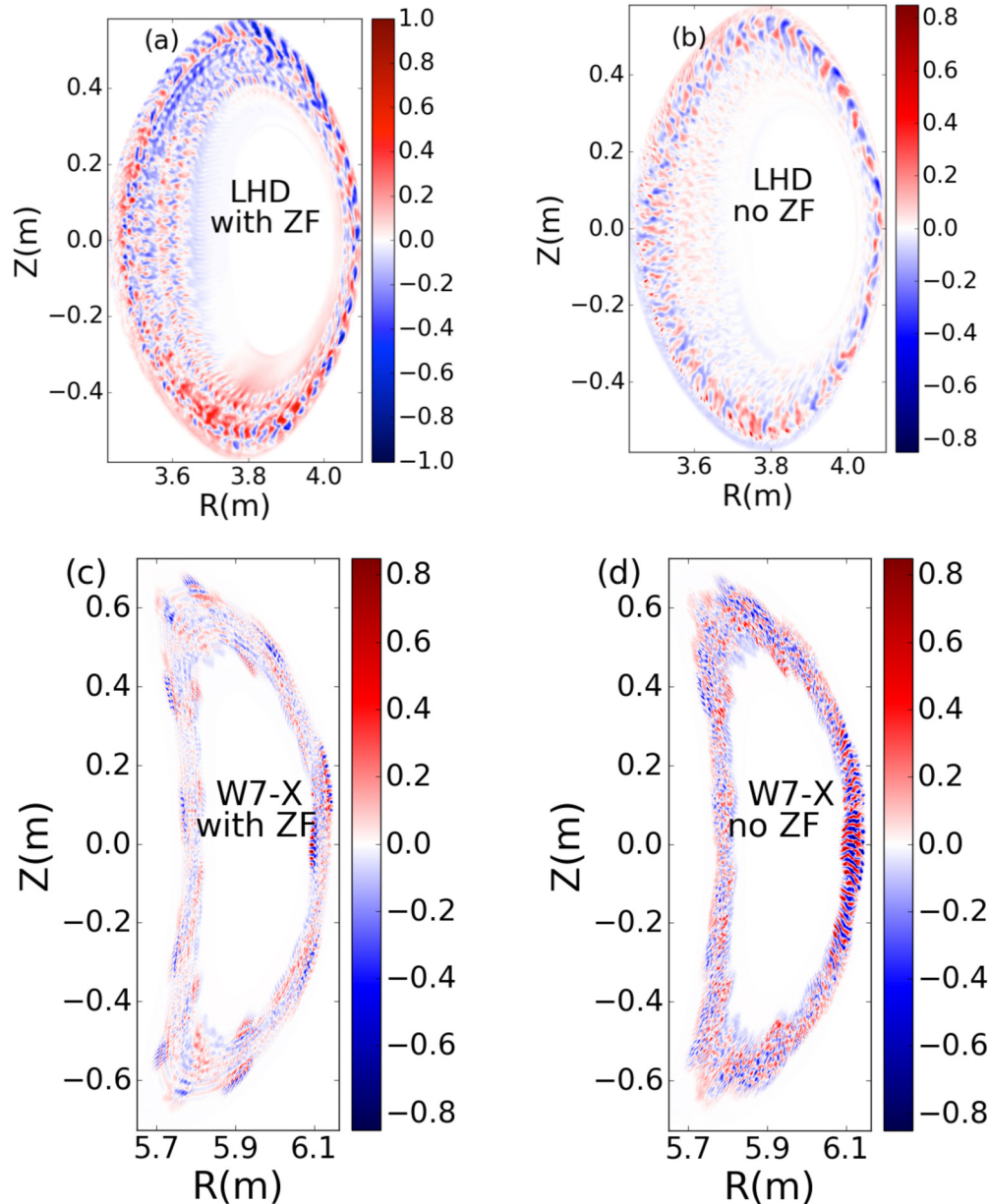


FIG. 8. Poloidal contour plots of non-zonal electrostatic potential $\delta\phi$ in the LHD from GTC simulations (a) with zonal flows and (b) without zonal flows at $t = 50R0/Cs$ and in the W7-X (c) with zonal flows and (d) without zonal flows $t = 30R0/Cs$.

ion heat conductivity χ_i is normalized by $\chi_{GB} = \chi_B \rho^*$, $\chi_B = cT_e/eB$, and $\rho^* = v_i m_i c / eBa$. Here, $v_i = \sqrt{T_i/m_i}$, and a is the minor radius. Turbulence amplitude $\delta\phi_{RMS}$ (defined as the root mean square of the non-zonal component) and transport χ_i first increase exponentially in the linear phase and then saturate in the nonlinear phase in simulations with and without zonal flows. Before the ITG nonlinear saturation, zonal flows grow exponentially with a growth rate similar to that of the turbulence intensity and ion heat conductivity (i.e., about two times the ITG linear growth rate). Figure 7 shows that when zonal flows are artificially suppressed, the saturation level of the turbulence amplitude and the ion heat conductivity are much larger than that when zonal flows are kept in the simulations, i.e., zonal flows greatly reduce the ITG turbulence amplitude and ion heat conductivity for both the LHD and W7-X. These initial nonlinear results support the view that turbulence-generated zonal flows¹⁸ can dominate the ITG instability saturation and suppress turbulent transport in toroidal plasmas. The zonal flows reduce the ion heat conductivity by a factor of about 20 and reduce the fluctuation amplitude by a factor of about 5 for both the LHD and W7-X. The ion heat conductivity in the LHD is slightly lower than that in the W7-X (after normalized by corresponding gyroBohm values), consistent with the fact that the linear growth in the LHD is slightly lower than that in the W7-X. However, we should point out that the plasma profiles used in these simulations are not realistic and the physics model is not complete (e.g., adiabatic electrons and only a single eigenmode family). We will perform more realistic nonlinear simulations in the future to compare simulation results with experiments and to assess the relative transport properties between the W7-X and LHD.

The comparisons of ITG non-zonal electrostatic potentials on the poloidal plane from simulations with and without self-generated zonal flows are given in Fig. 8. In the nonlinear phase, the radially elongated eigenmode structures are broken and the turbulence eddy size is reduced by zonal flows, which suppress the ion heat transport in both the LHD and W7-X. The effects of zonal flows appear to be slightly more pronounced for reducing the turbulence eddy sizes in the W7-X than in the LHD for the simulated equilibrium geometry and plasma profiles. The differences in the magnetic geometry and the ITG instability drive may contribute to the differences in the effects of zonal flows in regulating the ITG turbulence in the LHD and W7-X.

By comparing Fig. 8 with Figs. 2(c) and 5(c), we can see that the radial widths of the fluctuation intensity in both the LHD and W7-X are significantly broadened from the linear phase to the nonlinear phase (regardless of the zonal flows). This nonlinear broadening is clear from the time evolution of the radial profiles of the electrostatic potential amplitude in the simulation of the ITG with zonal flows in the W7-X as shown in Fig. 9(a). The radial widths of the fluctuation amplitude are much smaller than the simulation domain and nearly identical at different times (e.g., $t = 15R_0/C_s$ and $t = 20R_0/C_s$) during the linear phase but broaden significantly to the whole simulation domain at $t = 35R_0/C_s$ during the nonlinear phase. The broadening effects come from the turbulence spreading as demonstrated by the time history of the fluctuation amplitude in Fig. 9(b). The amplitude of the electrostatic potential $\delta\phi$ on a flux surface ($R = 6.12$ m) inside the linear eigenmode first increases exponentially with the linear growth rate γ_{GTC} and then saturates at $t = 23R_0/C_s$. In contrast, the amplitude of the electrostatic potential $\delta\phi$ on a flux surface ($R = 6.15$ m) outside the linear eigenmode does not increase exponentially.

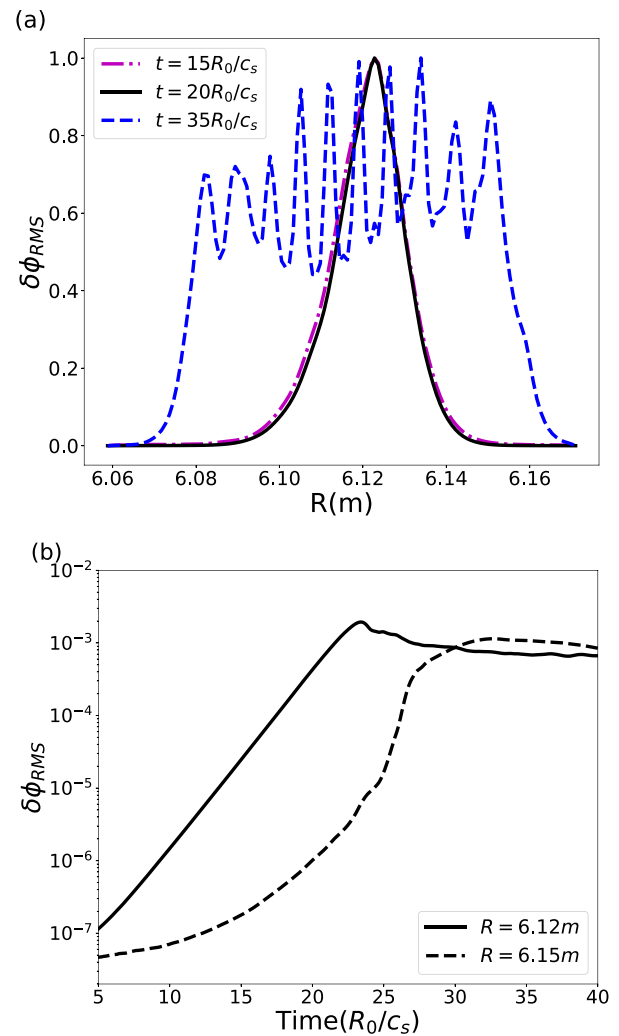


FIG. 9. (a) The radial profiles of electrostatic potential $\delta\phi_{RMS}$, normalized by the maximal value at $t = 15R_0/C_s$ and $t = 20R_0/C_s$ during the linear phase and at $t = 35R_0/C_s$ during the nonlinear phase in GTC simulation of the ITG with zonal flows in W7-X. (b) Time evolution of electrostatic potential $\delta\phi_{RMS}$ at a flux surface inside ($R = 6.12$ m, solid line) and at a flux surface outside ($R = 6.15$ m, dashed line).

It first increases slowly before $t = 15R_0/C_s$ but later increases much faster than the linear growth rate γ_{GTC} after $t = 25R_0/C_s$. We note that turbulence spreading was first observed in GTC global simulations of ITG turbulence in tokamaks²⁸ and can only be captured by radially nonlocal simulations such as these GTC global simulations performed in the current work.

The 2D spectra of the non-zonal electrostatic potential in the nonlinear phase are shown in Fig. 10, and the toroidal spectra (averaged over the radial domain) are shown in Fig. 11. In both the LHD and W7-X, the fluctuation spectra of the non-zonal modes ($n > 0$) exhibit an inverse cascade, where the spectral energy flows from high n and m harmonics in the linear phase to low n and m harmonics in the nonlinear phase. The nonlinear evolution of the potential spectra

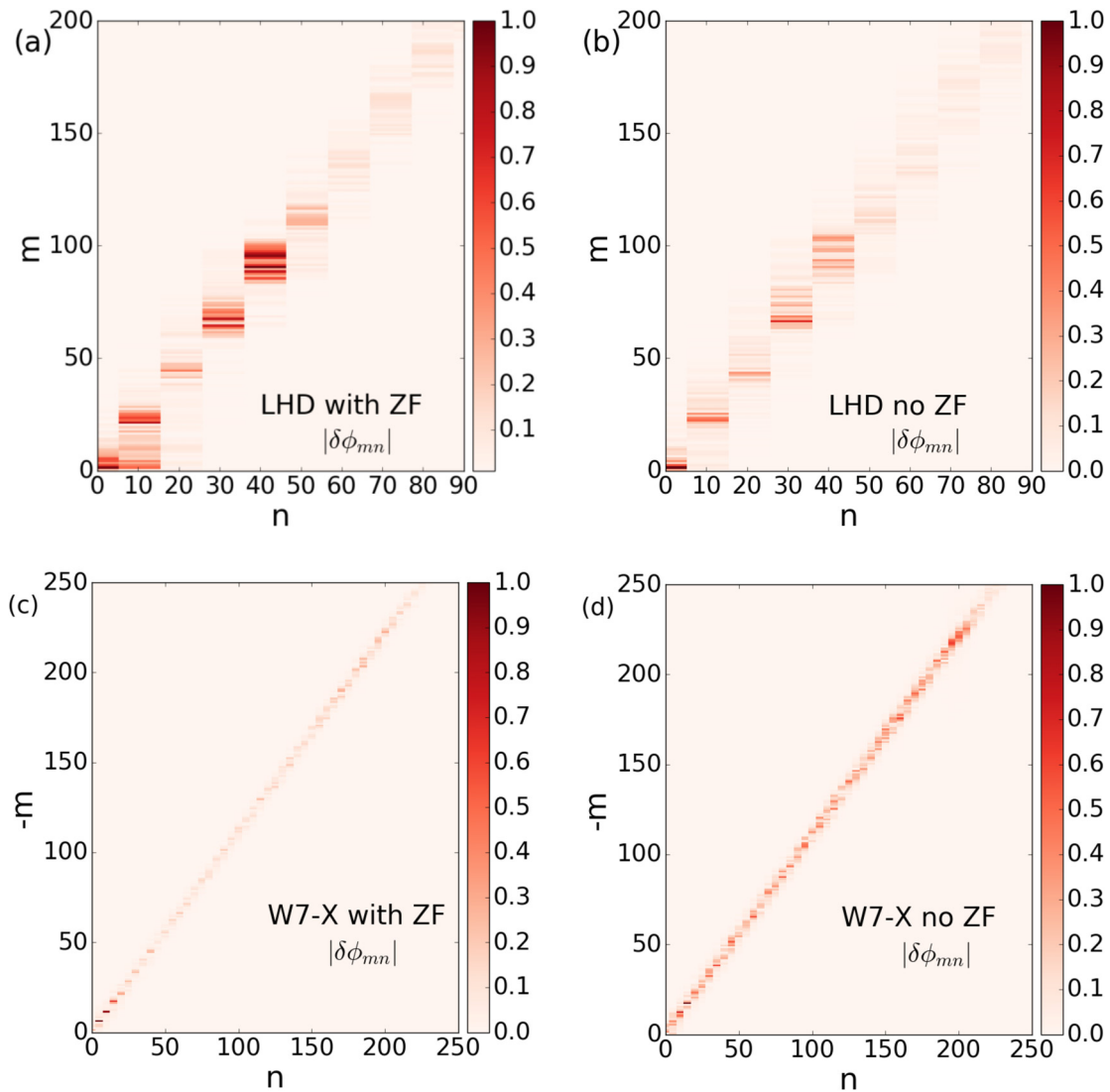


FIG. 10. Nonlinear 2D spectrum $|\delta\phi_{mn}|$ on the diagnosed flux surface of non-zonal electrostatic potential at $t = 50R_0/C_s$ in the LHD from GTC simulations (a) with zonal flow and (b) without zonal flow and at $t = 30R_0/C_s$ in the W7-X (c) with zonal flow and (d) without zonal flow.

would presumably indicate similar evolution of the heat conductivity induced by individual toroidal harmonic since the radial correlation length of individual toroidal harmonic would be similarly reduced by zonal flows.

Effects of zonal flows on the inverse cascade are quantitatively different between the LHD and W7-X. In the simulations of the LHD with or without zonal flows, the nonlinear spectra of the non-zonal modes contain both low- n and high- n components (up to linearly dominant $n = 40$ and $m = 92$ harmonic), as shown in Figs. 10(a) and 10(b) and Figs. 11(a) and 11(b). In the simulation of the W7-X without zonal flows, the nonlinear spectra also contain both low- n and high- n components (up to linearly dominant $n = 200$ and $m = -219$ harmonic), as shown in Figs. 10(d) and 11(d), and are dominant by

high- n components. In contrast, in the simulation of the W7-X with zonal flows, the nonlinear spectra contain low- n and high- n components but are dominated by low- n harmonics $n = 5, 10, 15$, which can be generated both by nonlinear toroidal coupling⁵³ of high- n harmonics (e.g., $n = 200$ and $n = 205$) and by linear toroidal coupling of these low- n harmonics with large amplitude zonal flows. The fact that the nonlinear low- n harmonics are more prominent in the W7-X than in the LHD is consistent with the linear eigenmode coupling more toroidal harmonics in the W7-X than in the LHD. Note that the linear toroidal coupling of zonal flows ($n = m = 0$) with non-zonal modes ($n > 0$) is induced by the magnetic field variation along the toroidal direction in stellarators, which is an interesting new physics mechanism absent in the axisymmetric tokamaks.

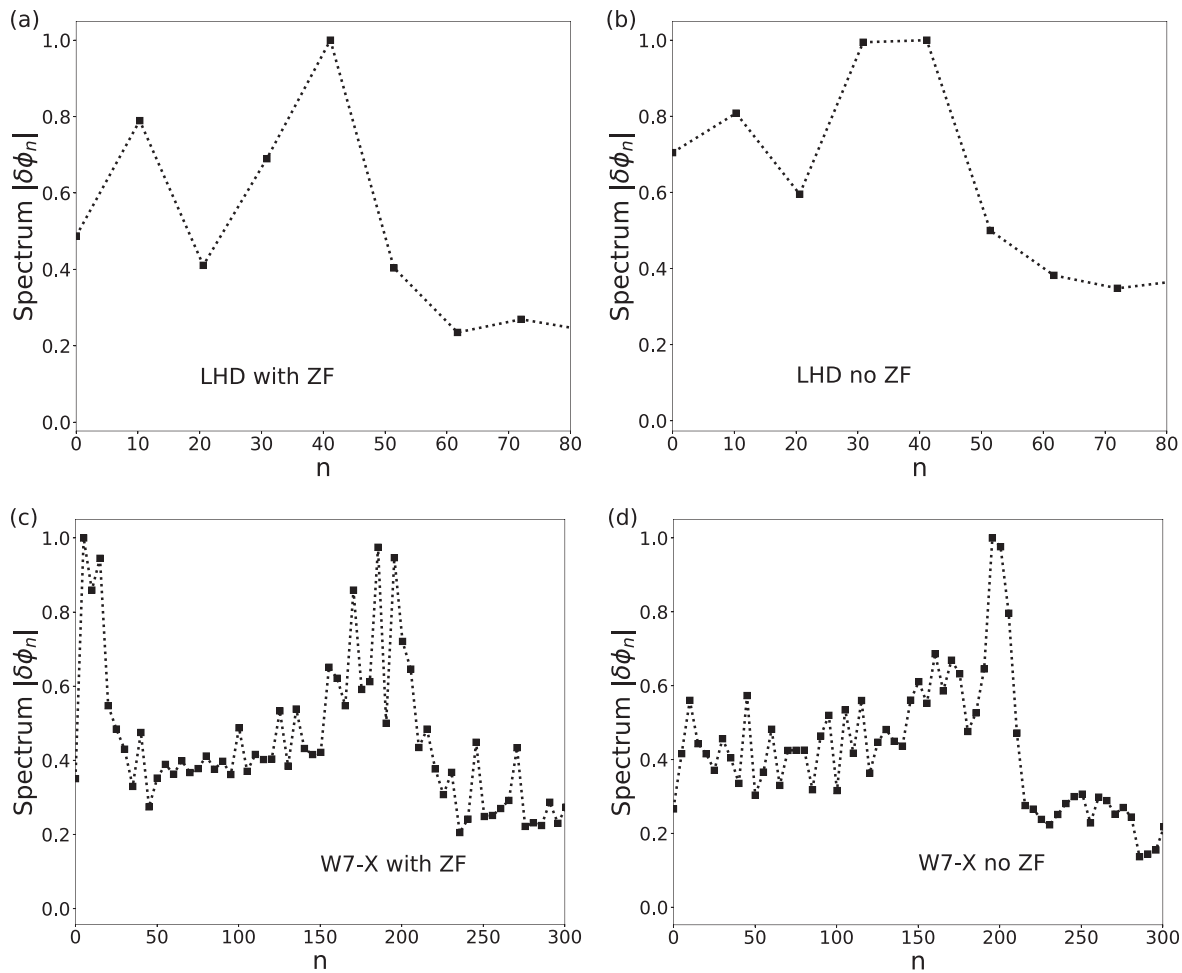


FIG. 11. Nonlinear toroidal spectrum $|\delta\phi_n|$ of non-zonal electrostatic potential averaged over the radial domain from GTC simulations at $50R_0/Cs$ in the LHD (a) with zonal flow and (b) without zonal flow and at $30R_0/Cs$ in the W7-X (c) with zonal flow and (d) without zonal flow.

V. CONCLUSION AND DISCUSSION

In conclusion, we have carried out both linear and nonlinear simulations of the ion temperature gradient (ITG) instability in the LHD and W7-X stellarators. Linear GTC simulations show that electrostatic ITG eigenmode structure is extended in the magnetic field direction but narrow in the perpendicular direction and peaks in bad curvature regions in both the LHD and W7-X. The eigenmode structure is localized at the outer mid-plane in the LHD, similar to that in a tokamak. On the other hand, the eigenmode structure in the W7-X is strongly localized to some magnetic fieldlines or within some discrete locations on the poloidal plane, which is due to the mirror-like magnetic fields varying strongly in the toroidal direction that inducing coupling of more toroidal n harmonics to form the linear eigenmode structure.

GTC nonlinear electrostatic simulations show that regulation by self-generated zonal flows is the dominant saturation mechanism for the ITG instabilities in both the LHD and W7-X. Furthermore, radial widths of the fluctuation intensity in both the LHD and W7-X are significantly broadened from the linear phase to the nonlinear phase due

to turbulence spreading. Finally, in the W7-X simulation with zonal flows, the nonlinear spectra are dominated by low- n harmonics, which can be generated both by nonlinear coupling of high- n harmonics and by linear toroidal coupling of these low- n harmonics with large amplitude zonal flows.

In the future work, we plan to study the effects of equilibrium radial electric fields (which require radially nonlocal simulations), kinetic electrons (e.g., trapped electron mode), nonlinear interactions with all eigenmode families (ten in the LHD and five in the W7-X) kept in simulations of stellarators, as well as interactions between neoclassical transport (which generates ambipolar radial electric fields) and microturbulence in stellarators.

ACKNOWLEDGMENTS

The authors would like to thank J. Riemann and R. Kleiber for performing EUTERPE simulations in a careful benchmark and for providing EUTERPE results including the frequency, growth rate,

and mode structure in Fig. 5. We acknowledge technical support by the GTC team. This work was supported by the China National Magnetic Confinement Fusion Science Program (Grant No. 2018YFE0304100); the U.S. Department of Energy, Office of Science, Office of Advanced Scientific Computing Research and Office of Fusion Energy Sciences, Scientific Discovery through Advanced Computing (SciDAC) program under Award Number DE-SC0018270 (SciDAC ISEP Center); and the China Scholarship Council (Grant No. 201806010067). This work used the resources of the Oak Ridge Leadership Computing Facility at the Oak Ridge National Laboratory (DOE Contract No. DE-AC05-00OR22725) and the National Energy Research Scientific Computing Center (DOE Contract No. DE-AC02-05CH11231).

DATA AVAILABILITY

The data that support the findings of this study are available from the corresponding author upon reasonable request.

REFERENCES

- ¹L. Spitzer, Jr., "The stellarator concept," *Phys. Fluids* **1**(4), 253–264 (1958).
- ²A. H. Boozer, "Non-axisymmetric magnetic fields and toroidal plasma confinement," *Nucl. Fusion* **55**(2), 025001 (2015).
- ³D. A. Spong, "3D toroidal physics: Testing the boundaries of symmetry breaking," *Phys. Plasmas* **22**(5), 055602 (2015).
- ⁴A. Dinklage, C. D. Beidler, P. Helander, G. Fuchert, H. Maassberg, K. Rahbarnia, T. Andreeva *et al.*, "Magnetic configuration effects on the Wendelstein 7-X stellarator," *Nat. Phys.* **14**(8), 855 (2018).
- ⁵M. Osakabe, Y. Takeiri, T. Morisaki, G. Motojima, K. Ogawa, M. Isobe, H. Takahashi *et al.*, "Current status of large helical device and its prospect for deuterium experiment," *Fusion Sci. Technol.* **72**(3), 199–210 (2017).
- ⁶S. Murakami, A. Wakasa, H. Maaßberg, C. D. Beidler, H. Yamada, K. Y. Watanabe, and LHD Experimental Group, "Neoclassical transport optimization of LHD," *Nucl. Fusion* **42**(11), L19 (2002).
- ⁷J. P. Freidberg, *Ideal MHD* (Cambridge University Press, 2014).
- ⁸M. Y. Isaev, J. Nührenberg, M. I. Mikhailov, W. A. Cooper, K. Y. Watanabe, M. Yokoyama, V. D. Shafranov *et al.*, "A new class of quasi-omnigenous configurations," *Nucl. Fusion* **43**(10), 1066 (2003).
- ⁹N. A. Pablant, A. Langenberg, A. Alonso, C. D. Beidler, M. Bitter, S. Bozhakov, G. Fuchert *et al.*, "Core radial electric field and transport in Wendelstein 7-X plasmas," *Phys. Plasmas* **25**(2), 022508 (2018).
- ¹⁰O. Grulke, "Plasma dynamics and transport studies in Wendelstein 7-X," in 27th IAEA Fusion Energy Conference (FEC 2018) (2018).
- ¹¹E. M. Edlund, M. Porkolab, Z. Huang, O. Grulke, L. G. Böttger, C. Von Sehren, and A. Von Stechow, "Overview of the Wendelstein 7-X phase contrast imaging diagnostic," *Rev. Sci. Instrum.* **89**(10), 10E105 (2018).
- ¹²M. Nakata, M. Nunami, H. Sugama, and T. H. Watanabe, "Isotope effects on trapped-electron-mode driven turbulence and zonal flows in helical and tokamak plasmas," *Phys. Rev. Lett.* **118**(16), 165002 (2017).
- ¹³M. J. Pueschel, B. J. Faber, J. Citrin, C. C. Hegna, P. W. Terry, and D. R. Hatch, "Stellarator turbulence: Subdominant eigenmodes and quasilinear modeling," *Phys. Rev. Lett.* **116**(8), 085001 (2016).
- ¹⁴P. Xanthopoulos, A. Mischchenko, P. Helander, H. Sugama, and T. H. Watanabe, "Zonal flow dynamics and control of turbulent transport in stellarators," *Phys. Rev. Lett.* **107**(24), 245002 (2011).
- ¹⁵H. E. Mynick, N. Pomphrey, and P. Xanthopoulos, "Reducing turbulent transport in toroidal configurations via shaping," *Phys. Plasmas* **18**(5), 056101 (2011).
- ¹⁶J. Riemann, R. Kleiber, and M. Borchardt, "Effects of radial electric fields on linear ITG instabilities in W7-X and LHD," *Plasma Phys. Controlled Fusion* **58**(7), 074001 (2016).
- ¹⁷S. Matsuoka, Y. Idomura, and S. Satake, "Neoclassical transport benchmark of global full-f gyrokinetic simulation in stellarator configurations," *Phys. Plasmas* **25**(2), 022510 (2018).
- ¹⁸Z. Lin, T. S. Hahm, W. W. Lee, W. M. Tang, and R. B. White, "Turbulent transport reduction by zonal flows: Massively parallel simulations," *Science* **281**(5384), 1835–1837 (1998).
- ¹⁹D. A. Spong, I. Holod, Y. Todo, and M. Osakabe, "Global linear gyrokinetic simulation of energetic particle-driven instabilities in the LHD stellarator," *Nucl. Fusion* **57**(8), 086018 (2017).
- ²⁰I. Holod, Z. Lin, S. Taimourzadeh, R. Nazikian, D. Spong, and A. Wingen, "Effect of resonant magnetic perturbations on microturbulence in DIII-D pedestal," *Nucl. Fusion* **57**(1), 016005 (2017).
- ²¹G. Dong and Z. Lin, "Effects of magnetic islands on bootstrap current in toroidal plasmas," *Nucl. Fusion* **57**(3), 036009 (2017).
- ²²K. S. Fang and Z. Lin, "Global gyrokinetic simulation of microturbulence with kinetic electrons in the presence of magnetic island in tokamak," *Phys. Plasmas* **26**(5), 052510 (2019).
- ²³P. Jiang, Z. Lin, I. Holod, and C. Xiao, "Effects of magnetic islands on drift wave instability," *Phys. Plasmas* **21**(12), 122513 (2014).
- ²⁴A. Reiman, G. Fu, S. Hirshman, L. Ku, D. Monticello, H. Mynick, A. Boozer *et al.*, "Physics design of a high-quasi-axisymmetric stellarator," *Plasma Phys. Controlled Fusion* **41**(12B), B273 (1999).
- ²⁵G. H. Neilson, A. H. Reiman, M. C. Zarnstorff, A. Brooks, G. Y. Fu, R. J. Goldston, H. Mynick *et al.*, "Physics issues in the design of high-beta, low-aspect-ratio stellarator experiments," *Phys. Plasmas* **7**(5), 1911–1918 (2000).
- ²⁶A. Reiman, L. Ku, D. Monticello, S. Hirshman, S. Hudson, C. Kessel, A. Boozer *et al.*, "Recent advances in the design of quasisymmetric stellarator plasma configurations," *Phys. Plasmas* **8**(5), 2083–2094 (2001).
- ²⁷J. L. Lewandowski, J. Williams, A. H. Boozer, and Z. Lin, "Gyrokinetic calculations of the neoclassical radial electric field in stellarator plasmas," *Phys. Plasmas* **8**(6), 2849–2854 (2001).
- ²⁸Z. Lin, S. Ethier, T. S. Hahm, and W. M. Tang, "Size scaling of turbulent transport in magnetically confined plasmas," *Phys. Rev. Lett.* **88**(19), 195004 (2002).
- ²⁹Y. Xiao, I. Holod, Z. Wang, Z. Lin, and T. Zhang, "Gyrokinetic particle simulation of microturbulence for general magnetic geometry and experimental profiles," *Phys. Plasmas* **22**(2), 022516 (2015).
- ³⁰I. Holod, D. Fulton, and Z. Lin, "Microturbulence in DIII-D tokamak pedestal—II. Electromagnetic instabilities," *Nucl. Fusion* **55**(9), 093020 (2015).
- ³¹L. L. Lao, J. M. Greene, T. S. Wang, F. J. Helton, and E. M. Zawadzki, "Three-dimensional toroidal equilibria and stability by a variational spectral method," *Phys. Fluids* **28**(3), 869–877 (1985).
- ³²S. P. Hirshman and J. C. Whitson, "Steepest-descent moment method for three-dimensional magnetohydrodynamic equilibria," *Phys. Fluids* **26**(12), 3553–3568 (1983).
- ³³N. M. Ferraro and S. C. Jardin, "Calculations of two-fluid magnetohydrodynamic axisymmetric steady-states," *J. Comput. Phys.* **228**(20), 7742–7770 (2009).
- ³⁴L. Galeotti, D. C. Barnes, F. Ceccherini, and F. Pegoraro, "Plasma equilibria with multiple ion species: Equations and algorithm," *Phys. Plasmas* **18**(8), 082509 (2011).
- ³⁵A. H. Boozer, "Plasma equilibrium with rational magnetic surfaces," *Phys. Fluids* **24**(11), 1999–2003 (1981).
- ³⁶F. Dubeau and J. Savoie, "Periodic quadratic spline interpolation," *J. Approximation Theory* **39**(1), 77–88 (1983).
- ³⁷W. W. Lee, "Gyrokinetic particle simulation model," *J. Comput. Phys.* **72**(1), 243–269 (1987).
- ³⁸A. J. Brizard and T. S. Hahm, "Foundations of nonlinear gyrokinetic theory," *Rev. Mod. Phys.* **79**(2), 421–468 (2007).
- ³⁹S. E. Parker and W. W. Lee, "A fully nonlinear characteristic method for gyrokinetic simulation," *Phys. Fluids B* **5**(1), 77–86 (1993).
- ⁴⁰Z. Lin, W. M. Tang, and W. W. Lee, "Gyrokinetic particle simulation of neoclassical transport," *Phys. Plasmas* **2**(8), 2975–2988 (1995).
- ⁴¹I. Holod, W. L. Zhang, Y. Xiao, and Z. Lin, "Electromagnetic formulation of global gyrokinetic particle simulation in toroidal geometry," *Phys. Plasmas* **16**(12), 122307 (2009).
- ⁴²R. B. White and M. S. Chance, "Hamiltonian guiding center drift orbit calculation for plasmas of arbitrary cross section," *Phys. Fluids* **27**(10), 2455–2467 (1984).
- ⁴³S. Okamura and Y. Suzuki, "Comparative study of magnetic field configurations of LHD and CHS based on the boundary shape analysis," *Plasma Fusion Res.* **6**, 2403048–2403048 (2011).

- ⁴⁴M. Wakatani, *Stellarator and Heliotron Devices* (Oxford University Press on Demand, 1998), Vol. 95.
- ⁴⁵T. H. Watanabe, H. Sugama, and S. Ferrando-Margalet, "Reduction of turbulent transport with zonal flows enhanced in helical systems," *Phys. Rev. Lett.* **100**(19), 195002 (2008).
- ⁴⁶K. Toi, F. Watanabe, K. Tanaka, T. Tokuzawa, K. Ogawa, M. Isobe, M. Osakabe, Y. Suzuki, T. Akiyama, K. Ida *et al.*, "Role of low-order rational surfaces in transport barrier formation on the large helical device," 23th IAEA Fusion Energy Conference, Daejeon, Korea, 11–16 October (2010).
- ⁴⁷J. Bao, Z. Lin, A. Kuley, and Z. X. Wang, "Nonlinear electromagnetic formulation for particle-in-cell simulation of lower hybrid waves in toroidal geometry," *Phys. Plasmas* **23**(6), 062501 (2016).
- ⁴⁸P. Cuthbert, J. L. V. Lewandowski, H. J. Gardner, M. Persson, D. B. Singleton, R. L. Dewar, W. A. Cooper *et al.*, "Toroidally localized and nonlocalized ballooning instabilities in a stellarator," *Phys. Plasmas* **5**(8), 2921–2931 (1998).
- ⁴⁹J. Riemann and R. Kleiber, private communication (2018).
- ⁵⁰M. D. J. Cole, R. Hager, T. Moritaka, J. Dominski, R. Kleiber, S. Ku, S. Lazerson, J. Riemann, and C. S. Chang, "Verification of the global gyrokinetic stellarator code XGC-S for linear ion temperature gradient driven modes," *Phys. Plasmas* **26**, 082501 (2019).
- ⁵¹H. Sugama and T. H. Watanabe, "Dynamics of zonal flows in helical systems," *Phys. Rev. Lett.* **94**(11), 115001 (2005).
- ⁵²A. Mishchenko and R. Kleiber, "Zonal flows in stellarators in an ambient radial electric field," *Phys. Plasmas* **19**(7), 072316 (2012).
- ⁵³Z. Lin, L. Chen, and F. Zonca, "Role of nonlinear toroidal coupling in electron temperature gradient turbulence," *Phys. Plasmas* **12**, 056125 (2005).